

## RESEARCH ARTICLE

10.1002/2017JA024178

## Key Points:

- A 2-D general curvilinear PIC simulation code is developed
- Rising-tone chorus waves are successfully reproduced in the simulations
- The wave normal angle of chorus waves is increasing during their propagation toward higher-latitude regions along a curved field line

## Correspondence to:

Q. Lu and X. Wang,  
qmlu@ustc.edu.cn;  
xywang@physics.auburn.edu

## Citation:

Ke Y., X. Gao, Q. Lu, X. Wang, and S. Wang (2017), Generation of rising-tone chorus in a two-dimensional mirror field by using the general curvilinear PIC code, *J. Geophys. Res. Space Physics*, 122, 8154–8165, doi:10.1002/2017JA024178.

Received 22 MAR 2017

Accepted 18 JUL 2017

Accepted article online 25 JUL 2017

Published online 3 AUG 2017

## Generation of rising-tone chorus in a two-dimensional mirror field by using the general curvilinear PIC code

Yangguang Ke<sup>1,2</sup> , Xinliang Gao<sup>1,2</sup> , Quanming Lu<sup>1,2</sup> , Xueyi Wang<sup>3</sup> , and Shui Wang<sup>1,2</sup>

<sup>1</sup>CAS Key Laboratory of Geospace Environment, Department of Geophysics and Planetary Science, University of Science and Technology of China, Hefei, China, <sup>2</sup>Collaborative Innovation Center of Astronautical Science and Technology, Harbin, China, <sup>3</sup>Physics Department, Auburn University, Auburn, Alabama, USA

**Abstract** Recently, the generation of rising-tone chorus has been implemented with one-dimensional (1-D) particle-in-cell (PIC) simulations in an inhomogeneous background magnetic field, where both the propagation of waves and motion of electrons are simply forced to be parallel to the background magnetic field. In this paper, we have developed a two-dimensional (2-D) general curvilinear PIC simulation code and successfully reproduced rising-tone chorus waves excited from an anisotropic electron distribution in a 2-D mirror field. Our simulation results show that whistler waves are mainly generated around the magnetic equator and continuously gain growth during their propagation toward higher-latitude regions. The rising-tone chorus waves are observed off the magnetic equator, which propagate quasi-parallel to the background magnetic field with the wave normal angle smaller than 25°. Due to the propagating effect, the wave normal angle of chorus waves is increasing during their propagation toward higher-latitude regions along an enough curved field line. The chirping rate of chorus waves is found to be larger along a field line with a smaller curvature.

### 1. Introduction

Chorus waves are one of the most significant electromagnetic emissions in the Earth's magnetosphere, which are typically observed within the frequency range of 0.1 to 0.8  $f_{ce}$  (where  $f_{ce}$  is the equatorial electron gyro-frequency) [Burtis and Helliwell, 1969; Tsurutani and Smith, 1974, 1977; Meredith et al., 2001; Li et al., 2012]. There is usually a power gap near 0.5  $f_{ce}$ , separating chorus waves into two distinct spectral bands: lower band (0.1–0.5  $f_{ce}$ ) and upper band (0.5–0.8  $f_{ce}$ ) [Tsurutani and Smith, 1974; Koons and Roeder, 1990; Gao et al., 2016a, 2017]. Chorus waves typically exhibit rising or falling tones but are often accompanied by a hiss-like band in the frequency-time spectrogram [Pope, 1963; Cornilleau-Wehrlin et al., 1978; Koons, 1981; Santolik et al., 2009; Li et al., 2012; Gao et al., 2014a]. Besides typical chorus waves, the large-amplitude whistler mode chorus waves are also frequently observed in Van Allen radiation belts during magnetically active periods, which are found to be quasi-monochromatic [Cattell et al., 2008; Cully et al., 2008; Kellogg et al., 2011; Wilson et al., 2011]. Based on statistical results from Time History of Events and Macroscale Interactions during Substorms (THEMIS) probes, chorus waves in the inner magnetosphere are detected with an amplitude range extending from ~10 pT to ~1 nT [Li et al., 2011b, 2012; Gao et al., 2014b]. For lower band chorus waves, rising tones are mainly field aligned with the wave normal angle typically smaller than 30°, while falling tones are usually very oblique [Li et al., 2011a, 2012].

Chorus waves have been widely believed to play a key role in controlling electron dynamics in the Van Allen radiation belt [Horne et al., 2003; Bortnik and Thorne, 2007; Summers et al., 2007; Thorne, 2010]. Through efficient pitch angle scattering, chorus waves can remove abundant lower energy (0.1–30 keV) electrons from the magnetosphere, leading to enhanced electron precipitation into the Earth's atmosphere [e.g., Lorentzen et al., 2001; Thorne et al., 2005; Lam et al., 2010]. Both theoretical and observational evidences have shown that chorus waves are the most important candidate for causing Earth's diffuse auroral precipitation [e.g., Thorne et al., 2010; Ni et al., 2011a; Ni et al., 2011b]. Furthermore, acceleration by chorus waves is the primary source of relativistic electrons in the outer radiation belt, which can enhance the flux of relativistic electrons (MeV) by several orders within 1 day during geomagnetic storms [Summers et al., 1998; Meredith et al., 2001; Horne et al., 2005; Thorne et al., 2013]. The relativistic electron acceleration can result from the quasi-linear wave-particle interaction with low-amplitude whistler waves [e.g., Thorne et al., 2013; Li et al., 2014] or from the much faster nonlinear electron interaction (trapping and phase bunching) with large-amplitude whistler waves [Omura et al., 2007; Cattell et al., 2008; Agapitov et al., 2014; Artemyev et al., 2014, 2016; Foster et al., 2017].

The generation of chorus waves with frequency chirping (either rising or falling) has long been an attractive topic. Their primary source region is located in the vicinity of the geomagnetic equatorial plane between the plasmopause and magnetopause [LeDocq *et al.*, 1998; Lauben *et al.*, 2002; Santolik *et al.*, 2005; Li *et al.*, 2009]. It has been generally accepted that anisotropic electrons with energy of tens of keV provide the free energy to excite chorus waves in the Earth's magnetosphere [Nunn, 1971; Karpman *et al.*, 1974; Omura *et al.*, 2008, 2012; Shklyar and Matsumoto, 2009; Li *et al.*, 2010; Demekhov, 2011; Omura and Nunn, 2011; Nunn and Omura, 2012; Gao *et al.*, 2014a; Nunn and Omura, 2015]. Many previous works indicated that the frequency chirping of chorus waves should be resulted from nonlinear interactions between resonant electrons and a coherent whistler wave [Nunn, 1974; Nunn *et al.*, 1997; Omura and Matsumoto, 1982; Omura and Summers, 2006; Gao *et al.*, 2016b]. Omura *et al.* [2008] derived the relativistic second-order resonant condition for a field-aligned chorus wave with the frequency chirping and pointed out that nonlinear trapping of resonant electrons results in the formation of a resonant current, which causes the growth of rising-tone chorus waves. However, the generation process of chorus waves in a realistic magnetic field configuration with curved field lines still remains unclear.

Particle-in-cell (PIC) simulation model is a very promising way to investigate the nonlinear physics underlying the generation process of chorus waves. With a one-dimensional (1-D) PIC simulation model, Hikishima and Omura [2012] studied the excitation of rising-tone chorus waves by anisotropic electrons and also revealed the production of electron holes resulted from the nonlinear trapping of resonant electrons, which has been predicted by the nonlinear theory [Omura *et al.*, 2008]. Moreover, they confirmed the optimum condition for generating chorus waves, which is further supported by THEMIS observations [Gao *et al.*, 2014a]. With the same simulation model, Katoh and Omura [2013] investigated the effect of the background magnetic field inhomogeneity on the generation of rising-tone chorus waves and showed that the larger spatial inhomogeneity of the background magnetic field results in the larger threshold amplitude for the chorus excitation. In their simulation model, in order to include the mirror motion of electrons in the 1-D system, they used a cylindrical mirror field model when solving the motion equation of electrons. Moreover, due to the limitation of 1-D simulation model, both the propagation of chorus waves and motion of electrons are artificially forced to be along the background magnetic field, whereas chorus waves are typically observed with a finite wave normal angle in the magnetosphere, which indicates that both the generation and propagation of chorus waves should be studied in a 2-D simulation model.

In this paper, we develop a two-dimensional (2-D) general curvilinear PIC simulation code and perform it to study the generation of rising-tone chorus waves in the two-dimensional (2-D) mirror field. In this model, both the propagation of waves and motion of electrons are now allowed to cross the background magnetic field. The global distribution of the wave amplitude, frequency chirping rate, wave normal angle, and Poynting flux for the excited rising-tone chorus waves are thoroughly investigated with this code. In section 2, we will describe our simulation model in detail. The simulation results are presented in section 3. In section 4, we summarize and further discuss our principal results.

## 2. Simulation Model

In the present study, we develop a 2-D general curvilinear PIC simulation code to extend the existing 1-D self-consistent simulation model performed by Katoh and Omura [2006] and Tao [2014] and utilize this code to investigate the generation of rising-tone chorus in a 2-D mirror field. The mirror field is considered as the background magnetic field  $\mathbf{B}_0$  in our simulation system, and its three components in the Cartesian coordinate are

$$\begin{cases} B_{0x} = -2\xi x z B_{0eq}, \\ B_{0y} = 0, \\ B_{0z} = (1 + \xi z^2) B_{0eq}. \end{cases} \quad (1)$$

where  $B_{0eq}$  represents the magnetic field at  $z = 0$  (the magnetic equator) and  $\xi$  is a parameter representing the inhomogeneity of the background magnetic field. The background magnetic field satisfies  $\nabla \cdot \mathbf{B}_0 = 0$ , and the magnetic field line equation can be obtained by solving

$$\frac{dx}{B_{0x}} = \frac{dz}{B_{0z}}, \quad (2)$$

and it gives

$$x = \frac{x_0}{1 + \xi z^2}, \quad (3)$$

where  $x_0$  is the position of the magnetic field lines at  $z = 0$ . In our simulations, the electron population consists of two components: cold and hot components. The cold electrons are treated as a fluid, and hot electrons are modeled as kinetic particles considering the relativistic effect, which is the same as those used in the electron hybrid model of *Katoh and Omura* [2007]. Ions are assumed to be an immobile neutralizing component since the frequencies of the investigated chorus waves are much larger than the ion cyclotron frequency. The motions of cold electrons are governed by the following equations:

$$\begin{aligned} \frac{\partial n_c}{\partial t} &= -\nabla \cdot (n_c \mathbf{V}_c), \\ \frac{\partial \mathbf{V}_c}{\partial t} &= -(\mathbf{V}_c \cdot \nabla) \mathbf{V}_c + \frac{q_e}{m_e} (\mathbf{E} + \mathbf{V}_c \times \mathbf{B}), \\ \mathbf{J}_c &= q_e n_c \mathbf{V}_c, \end{aligned} \quad (4)$$

where the subscript “c” refers to the cold electron component,  $n$  is the electron number density,  $\mathbf{V}$  is the electron bulk velocity,  $\mathbf{J}$  is the electron current density, and  $\mathbf{B}$  and  $\mathbf{E}$  are the total magnetic and electric fields, respectively. The hot electrons move in the Lorentz force:

$$\frac{d(\gamma \mathbf{v}_h)}{dt} = \frac{q_e}{m_e} (\mathbf{E} + \mathbf{v}_h \times \mathbf{B}), \quad (5)$$

where the subscript “h” refers to the hot electron component,  $\mathbf{v}_h$  is the particle velocity of hot electrons, and  $\gamma = 1/\sqrt{1 - (|\mathbf{v}_h|/c)^2}$ . The total current density can be calculated by

$$\mathbf{J} = \mathbf{J}_c + q_e n_h \mathbf{V}_h, \quad (6)$$

where  $n_h$  is the hot electron number density and  $\mathbf{V}_h$  is the average velocity of hot electrons. Then, the magnetic and electric fields are updated by solving Maxwell equations:

$$\begin{aligned} \frac{\partial \mathbf{E}}{\partial t} &= \frac{1}{\mu_0 \epsilon_0} \nabla \times \mathbf{B} - \frac{1}{\epsilon_0} \mathbf{J}, \\ \frac{\partial \mathbf{B}}{\partial t} &= -\nabla \times \mathbf{E}. \end{aligned} \quad (7)$$

In our simulation, we deposit the charge density and current density to the grids, which automatically satisfies the charge conservation. Our simulation is performed in the  $x$ - $z$  plane. The simulation domain is divided into grids by a group of field lines  $x = x_0/(1 + \xi z^2)$  with equal spacing  $\Delta x_0$  at the magnetic equator and a group of lines  $z = z_0$  with equal spacing  $\Delta z_0$  as shown in Figure 1. The spatial scale in the simulation is normalized by  $\rho_{e0} = w_{\parallel|eq}/\Omega_{e0}$ , where  $w_{\parallel|eq}$  and  $\Omega_{e0}$  are the initial values of parallel thermal velocity of hot electrons and electron gyrofrequency at the magnetic equator, respectively. The domain boundaries are  $x = \pm 700\rho_{e0}/(1 + \xi z^2)$  and  $z = \pm 500\rho_{e0}$ . We move the particles in the Cartesian coordinate; however, the wave magnetic and electric fields are updated by solving Maxwell equations in the general curvilinear coordinate  $(p, w)$ :

$$\begin{cases} p = (1 + \xi z^2)x \\ w = z. \end{cases} \quad (8)$$

The scale factors are

$$h_p = \frac{1}{1 + \xi w^2} \quad \text{and} \quad h_w = \sqrt{(2\xi p w / (1 + \xi w^2))^2 + 1}. \quad (9)$$

Two types of boundary conditions are used in our simulation. Reflecting boundary conditions are used for particles. When a particle hits the  $x = \pm 700\rho_{e0}/(1 + \xi z^2)$  or  $z = \pm 500\rho_{e0}$  boundaries, its normal velocity (perpendicular to the boundary) reverses the direction. Absorbing boundary conditions are assumed for waves. A masking function is used to damp wave fields near the simulation boundary [Tao, 2014]. Initially, the cold

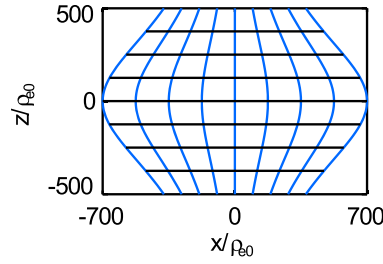


**Figure 1.** The sketch map of spatial grids of the simulation domain in the Cartesian coordinate  $(x, z)$ . The blue lines denote the magnetic field lines.

electrons are assumed to be distributed uniformly in the simulation domain. Their number density is  $n_{c0}$ , and bulk velocity is  $V_{c0} = 0$ . The plasma frequency of cold electrons is  $\omega_{pe} = 5\Omega_{e0}$ , where  $\omega_{pe} = \sqrt{n_{c0}e^2/m_e\epsilon_0}$ . For the hot electrons, at the magnetic equator ( $z = 0$ ), the number density is  $n_{heq}$ , and velocity distribution is bi-Maxwellian,

$$f_{eq}(v_{h||}, v_{h\perp}) = \frac{1}{(2\pi)^{3/2} w_{||eq} w_{\perp eq}^2} \exp\left(-\frac{v_{h||}^2}{2w_{||eq}^2} - \frac{v_{h\perp}^2}{2w_{\perp eq}^2}\right), \quad (10)$$

where  $w_{||eq}$  and  $w_{\perp eq}$  are the thermal velocities of hot electrons in the parallel and perpendicular directions, respectively. According to the force balance condition [Chan et al., 1994], the hot electron pressure is expressed as follows:

$$p_{||} = \frac{n_{heq} T_{||eq}}{\zeta}, \quad \text{and} \quad p_{\perp} = \frac{n_{heq} T_{\perp eq}}{\zeta^2}, \quad (11)$$

where  $\zeta = 1 + (T_{\perp eq}/T_{||eq} - 1)(1 - B_{0eq}/B_0)$ ,  $T_{||eq}$  and  $T_{\perp eq}$  are the parallel and perpendicular temperatures of hot electrons at the magnetic equator, respectively. Based on conservation of energy and the magnetic moment, the hot electron number density derived from direct integration of equation (10) has the following dependence:

$$n_h = n_{heq}/\zeta. \quad (12)$$

Then the hot electron temperature off the equator is given as follows:

$$T_{||} = T_{||eq}, \quad \text{and} \quad T_{\perp} = T_{\perp eq}/\zeta. \quad (13)$$

Therefore, the velocity distribution of hot electrons can be expressed as follows:

$$f(v_{h||}, v_{h\perp}) = \frac{1}{(2\pi)^{3/2} w_{||eq} w_{\perp eq}^2/\zeta} \exp\left(-\frac{v_{h||}^2}{2w_{||eq}^2}\right) \exp\left(-\frac{v_{h\perp}^2}{2w_{\perp eq}^2/\zeta}\right). \quad (14)$$

The initial settings of hot electrons at the magnetic equator are as follows: the number density is  $n_{heq} = 0.01 n_{c0}$ , the temperature anisotropy is  $T_{\perp eq}/T_{||eq} = 4.5$ , and the parallel beta  $\beta_{||} = n_{heq} T_{||eq}/(B_{0eq}^2/2\mu_0) = 0.01$ . The initial number density and temperature anisotropy of hot electrons are shown in Figure 2. Approximately 1.05 billion superparticles are used for hot electrons in our simulation. The parameters are summarized in Table 1.

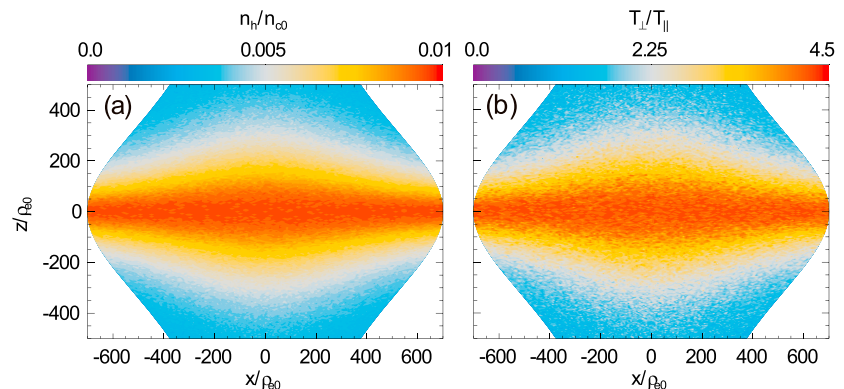


**Figure 2.** (a) Initial distribution of the hot electron number density  $n_h/n_{c0}$  and (b) the anisotropy of hot electrons  $T_{\perp}/T_{||}$  in the simulation domain.

Table 1. Simulation Parameters	
Parameters	Value
$\zeta$	$3.45 \times 10^{-6} \rho_{e0}^{-2}$
Density ratio $n_{heq}/n_{c0}$	0.01
Temperature anisotropy $T_{\perp eq}/T_{\parallel eq}$	4.5
Plasma frequency of cold electrons $\omega_{pe}$	$5\Omega_{e0}$
The parallel beta of hot electrons at the magnetic equator $\beta_{\parallel  e}$	0.01
Time step $\Delta t$	$0.02\Omega_{e0}^{-1}$
Grid spacing $\Delta x_0$	$1.37\rho_{e0}$
Grid spacing $\Delta z_0$	$0.49\rho_{e0}$

### 3. Simulation Results

The overview of our simulation results is presented in Figure 3, which shows spatial profiles of the  $\delta(T_{\perp}/T_{\parallel})$  and amplitude of fluctuating magnetic fields perpendicular to the background magnetic field  $B_{\perp}/B_{0eq}$  at  $\Omega_{e0}t = 400, 700,$  and  $1200,$  respectively. Here  $\delta(T_{\perp}/T_{\parallel}) = (T_{\perp}/T_{\parallel})_t - (T_{\perp}/T_{\parallel})_0$  is the variation of temperature anisotropy of hot electrons compared to the initial value. At  $\Omega_{e0}t = 400,$  the temperature anisotropy of hot electrons, which is considered as the energy source of chorus waves, begins to decrease at

the magnetic equator, as shown in Figure 3a. Just as expected, the fluctuating magnetic field also begins to grow from the magnetic equator in Figure 3b. With the time increasing, from  $\Omega_{e0}t = 400$  to  $1200,$  the decrease of the temperature anisotropy becomes more significant at the magnetic equator and also gradually expands to higher-latitude regions. Meanwhile, the fluctuating magnetic fields are firstly excited at the magnetic equator and then propagate up to the higher-latitude regions.

In order to further analyze the detailed frequency-time spectrogram of chorus waves and study effects from the inhomogeneity and curved configuration of the background magnetic field, we extract time series of fluctuating magnetic fields from 10 locations along two typical magnetic field lines L1 and L2, which have been marked by asterisks "\*" in Figure 3f. Figure 4 displays the frequency-time spectrogram of fluctuating magnetic fields perpendicular to the background magnetic field at these 10 locations ( $|z| = 0, 80, 160, 240,$  and  $320\rho_{e0}$

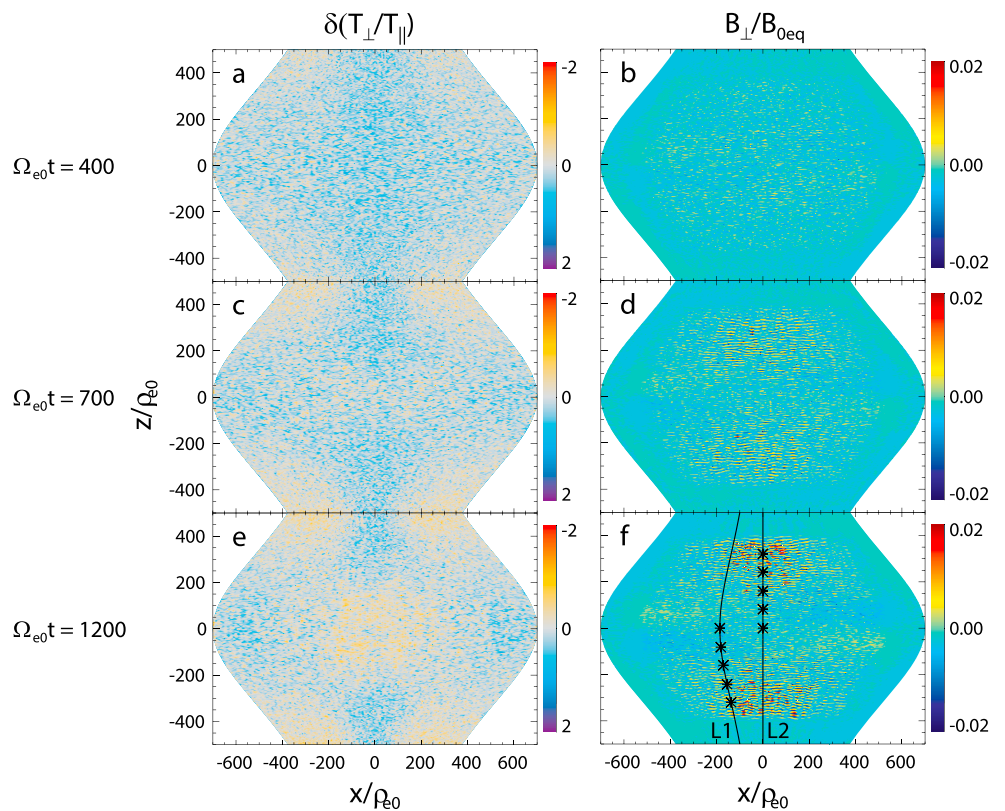


**Figure 3.** The spatial profiles of the disturbed anisotropy (a, c, and e)  $\delta(T_{\perp}/T_{\parallel})$  and perpendicular fluctuating magnetic fields (b, d, and f)  $B_{\perp}/B_{0eq}$  at  $\Omega_{e0}t = 400, 700,$  and  $1200,$  respectively. In Figure 3f, the curve and straight solid lines through  $(-186\rho_{e0}, 0)$  and  $(0, 0)$  represent two selected typical magnetic field lines marked by L1 and L2, respectively. Ten observation locations at  $|z| = 0, 80, 160, 240,$  and  $320\rho_{e0}$  along the field line L1 (L2) are denoted by asterisks "\*".

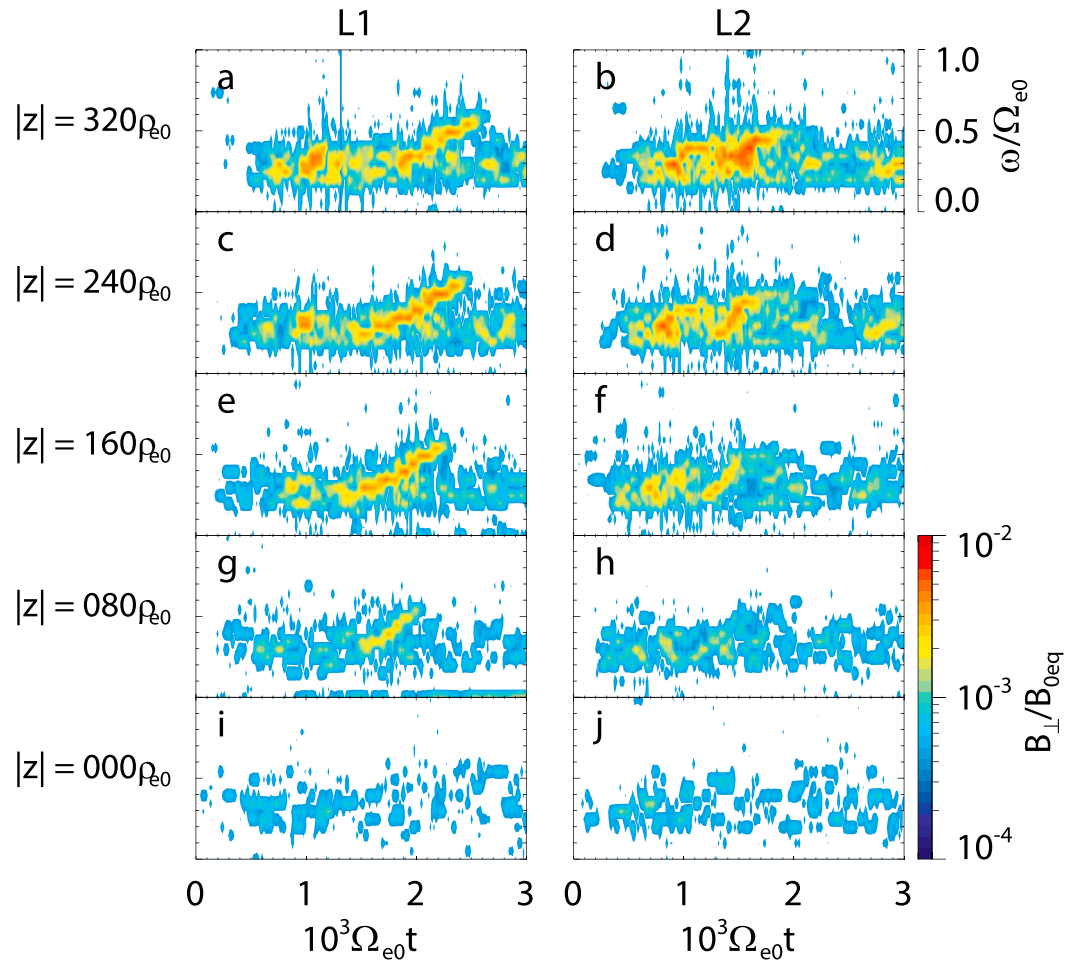


**Figure 4.** The frequency-time spectrogram of perpendicular fluctuating magnetic fields  $B_{\perp}/B_{0eq}$  at 10 selected locations along (a, c, e, g, and i) L1 and (b, d, f, h, and j) L2 as shown in Figure 3f.

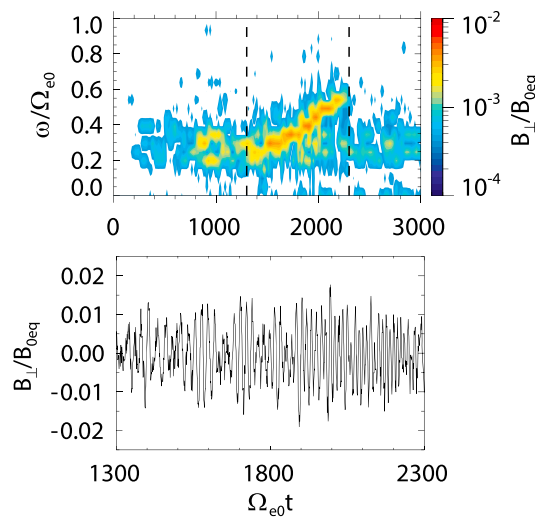


**Figure 5.** (top) Frequency-time spectrogram of rising-tone element at location  $z = -160\rho_{e0}$  along field line L1. (bottom) Wave packet from  $\Omega_{e0}t = 300$  to  $1100$  corresponding to the duration between the two vertical dashed lines plotted in Figure 5 (top).

along L1 and L2). At the magnetic equator (Figures 4i and 4j), there are only whistler mode waves, rather than chorus waves with the coherent structure. However, off the magnetic equator (Figures 4a–4f), there are clear rising-tone chorus elements excited in our simulation. Even though these two field lines are close to each other, we can still find one distinct difference between them: two chorus elements are observed along L2 (right column), but only one chorus elements can be found along L1 (left column). Figure 5 (top) presents one rising-tone element observed at location  $z = -160\rho_{e0}$  along field line L1 whose wave packet is exhibited in Figure 5 (bottom). The quasiperiodic modulation of the wave amplitude and the resulting subpackets can be observed, which are similar to the observations [Santolík *et al.*, 2003].

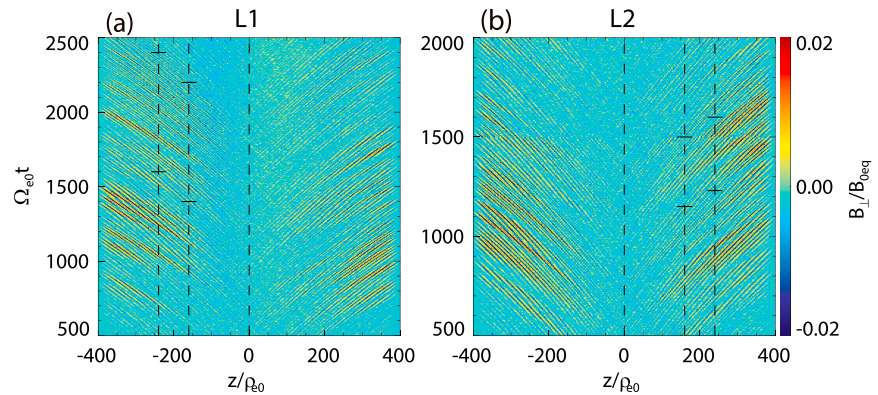


**Figure 6.** Temporal evolution of perpendicular fluctuating magnetic fields  $B_{\perp}/B_{0eq}$  along field lines (a) L1 and (b) L2. The short bars in two panels denote the start and end of rising-tone elements at locations  $|z| = 160$  and  $240\rho_{e0}$  along two field lines.

The evolution of fluctuating magnetic fields perpendicular to the background magnetic field along two field lines (L1 and L2) is illustrated in Figure 6. The short bars in Figures 6a and 6b denote the start and end of rising-tone elements at locations  $|z| = 160$  and  $240\rho_{e0}$  along two field lines. The main source of these chorus waves is from the magnetic equator region. Afterward, wave packets will propagate toward the polar region and their amplitudes are gradually enhanced. More interestingly, the wave packets confined within two short bars at  $|z| = 160$  and  $240\rho_{e0}$  seem to come from the same source region, i.e., the magnetic equator, which means that the rising-tone element is first formed at the magnetic equator but only with a negligible amplitude. Then, the rising-tone element will propagate away from the equator, and its amplitude will continuously increase up to the observable level.

The distribution of chirping rates of rising-tone elements is displayed in Figure 7. Here along both field lines (L1 and L2), we choose two typical locations ( $|z| = 160$  and  $240\rho_{e0}$ ) to estimate the chirping rate. In each panel, the black dotted line along the rising-tone element is a fitting of dominant frequencies with the maximum power at each time by the linear least square method. Then the chirping rate is just the slope of the black dotted line. The chirping rates  $\Gamma$  are estimated as  $3.7 \times 10^{-4}$ ,  $3.5 \times 10^{-4} \Omega_{e0}^2$  at  $z = -160, -240\rho_{e0}$  on L1 and as  $7.7 \times 10^{-4}$ ,  $7.6 \times 10^{-4} \Omega_{e0}^2$  at  $z = 160, 240\rho_{e0}$  on L2. With the same distance off the magnetic equator, the chirping rate of the rising-tone element along L1 is smaller than that along L2. Figure 8 presents the

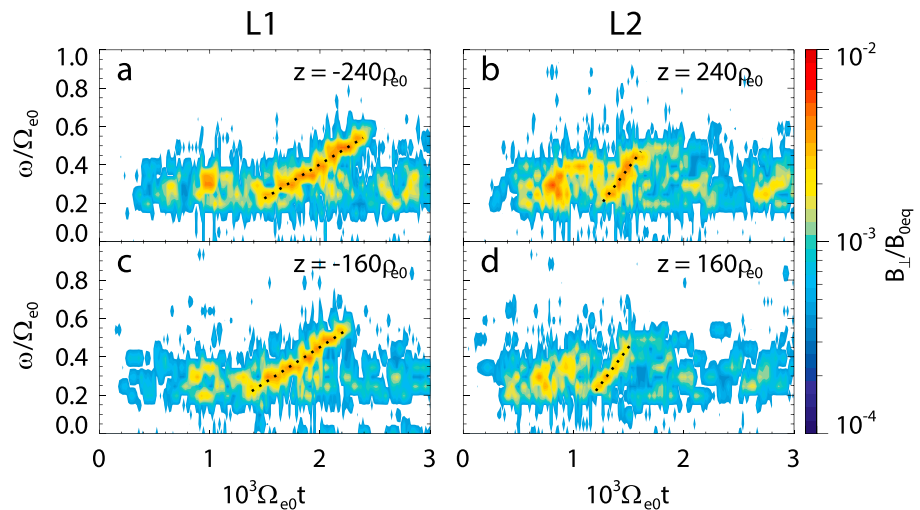


**Figure 7.** The frequency-time spectrogram of perpendicular fluctuating magnetic fields  $B_{\perp}/B_{0eq}$  at (a and c)  $|z| = 160$  and (b and d)  $240\rho_{e0}$  along L1 and L2, respectively. In each panel, the black dotted line along the rising-tone element is a fitting of dominant frequencies with the maximum power at each time by the linear least square method.

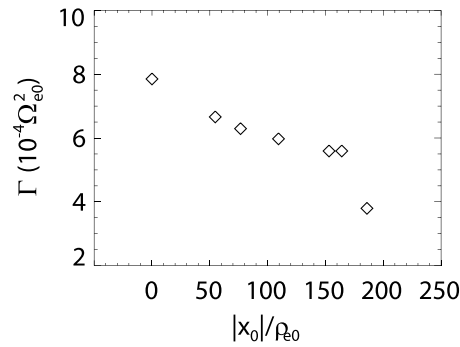


**Figure 8.** The distribution of the chirping rates  $\Gamma$  of rising-tone elements appearing at  $|z| = 160\rho_{e0}$  for different field lines. The  $|x_0|$  denotes the distance from these field lines to the middle field line at the equator.

distribution of the chirping rates  $\Gamma$  of rising-tone elements at  $|z| = 160\rho_{e0}$  along different field lines. The  $|x_0|$  denotes the distance from these field lines to the middle field line at the equator. There is a trend that the chirping rate decreases as  $|x_0|$  increases.

With the same format of Figure 4, Figure 9 shows the distribution of wave normal angles of rising-tone chorus along field lines L1 and L2 at 10 locations. For visual clarity, we only display wave normal angles  $\theta$  of wave modes whose wave power is larger than  $0.25P_{max}$ , where the  $P_{max}$  is the maximum of wave power at a fixed position during the simulation time. Furthermore, the average wave normal angles of rising-tone elements at different places along field lines (left) L1 and (right) L2 are displayed in Figure 10. The rising-tone elements along field line L2 are nearly field-aligned with the wave normal angles  $\theta \approx 8^\circ$  as seen in Figures 9b, 9d, 9f, 9h, 9j, and 10 (right). While the wave normal angles of chorus waves increase as the waves propagate toward higher-latitude regions along the curved field line L1 as shown in Figures 9a, 9c, 9e, 9g, 9i, and 10 (left). And the wave normal angles can increase up to  $\sim 25^\circ$  when the chorus waves reach the absorption region at  $|z| > 360\rho_{e0}$ .

We also consider the distribution of the Poynting flux in this paper. Figure 11 illustrates the parallel component of Poynting vector  $S_{||}/|S|$  of chorus emissions at 10 selected locations along two field lines L1 and L2, where  $|S|$  is the intensity of Poynting flux  $S$  for each wave mode. For visual clarity, we only display  $S_{||}/|S|$  of wave modes whose wave power is larger than  $0.04 P_{max}$ . At the magnetic equator,  $z=0$ , the waves are

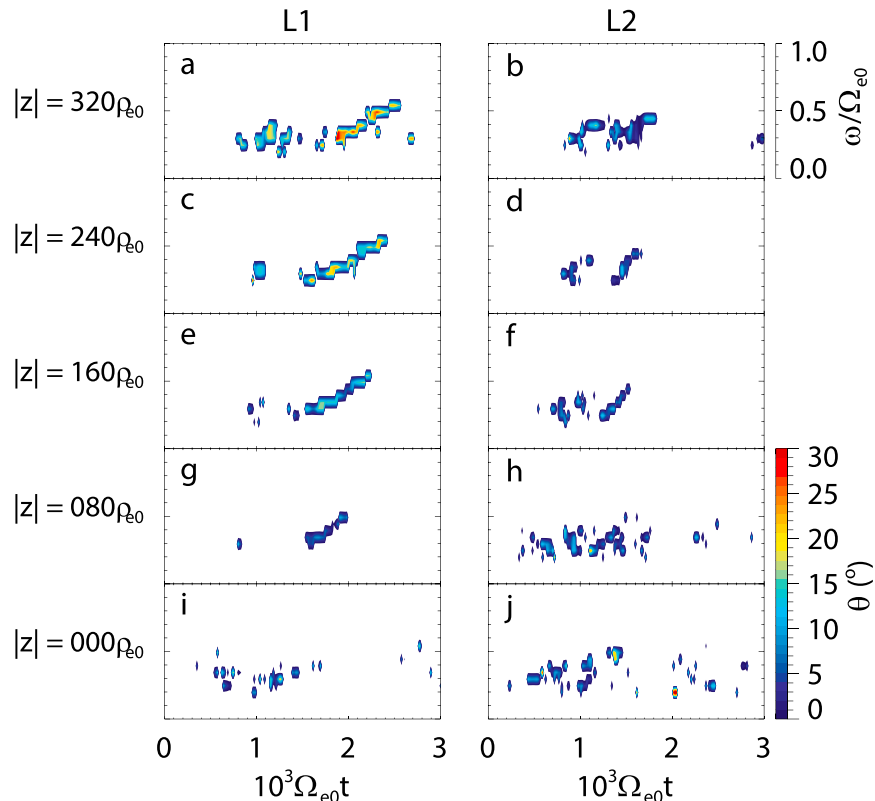


**Figure 9.** The distribution of the wave normal angle  $\theta$  at 10 selected locations along field lines (a, c, e, g, and i) L1 and (b, d, f, h, and j) L2.



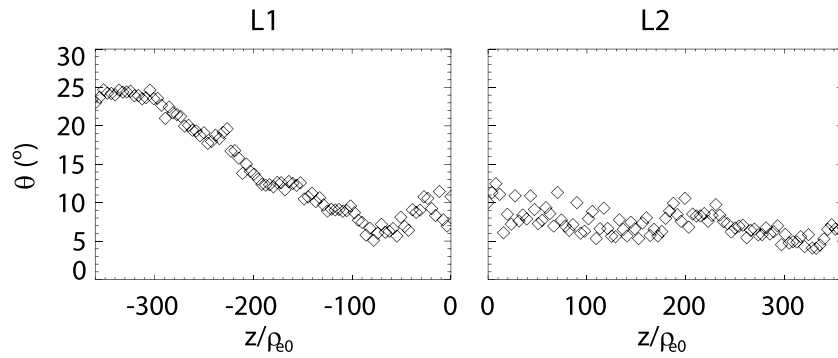


**Figure 10.** The average wave normal angle  $\theta$  of rising-tone elements at different locations along field lines (left) L1 and (right) L2.

propagating toward both upward and downward (Figures 11i and 11j), which is consistent with the prediction of the linear theory [Gary and Karimabadi, 2006]. At higher-latitude regions,  $|z|=80$  and  $160 \rho_{e0}$ , the waves are mainly propagating toward the polar region, but we can still find that some wave modes are propagating toward the magnetic equator (Figures 11e–11h). This indicates that the anisotropic electron distribution off the equator is also unstable to excite whistler waves, which is consistent with the expanded region of the declining anisotropy in Figure 3e. At even higher-latitude regions, the overwhelming majority of the waves propagate toward the polar region. It is worth noting that the rising-tone chorus remains the same propagating direction after it is excited at the magnetic equator.

#### 4. Summary and Discussion

In order to consider the effects of both the inhomogeneity and curved configuration of the background magnetic field on the evolution of chorus waves, we develop a 2-D general curvilinear PIC simulation code, where

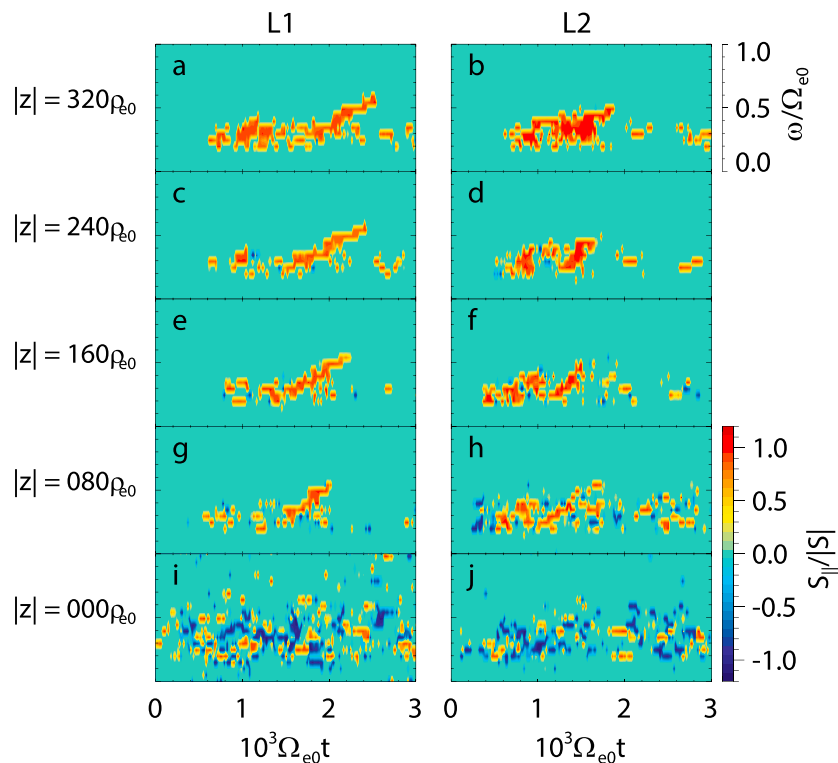


**Figure 11.** The distribution of the parallel component of Poynting vector  $S_{\parallel}/|S|$  at 10 selected locations along two field lines (a, c, e, g, and i) L1 and (b, d, f, h, and j) L2.

both the propagation of waves and motion of electrons are now allowed to cross the background magnetic field. We successfully reproduced rising-tone chorus waves excited by an anisotropic electron distribution in a 2-D mirror field. Our simulation results show that whistler waves are mainly generated around the magnetic equator and continuously gain growth during their propagation toward higher-latitude regions. The rising-tone chorus waves are observed off the magnetic equator, which propagate quasi-parallel to the background magnetic field with the wave normal angle smaller than  $25^\circ$ . There is a clear trend that the wave normal angles of chorus waves are increasing during their propagation toward higher-latitude regions along an enough curved field line. And the chirping rate of chorus waves is found to be larger along a field line more close to the middle field line.

In the theoretical work by *Helliwell* [1967], the change of  $\Gamma$  mainly depends on the intensity  $B_0$  and inhomogeneity  $dB_0/ds$  of the background field in the source region of chorus waves, where  $s$  is a distance along the field line from the equatorial plane. However, the variations of both  $B_0$  and  $dB_0/ds$  due to the different  $|x_0|$  in these source regions in our simulation are small and unable to account for the change of  $\Gamma$  over  $|x_0|$ . However, there is a clear trend that the magnetic amplitude of chorus waves will decrease with the distance  $|x_0|$  from the middle field line at the magnetic equator (not shown). Therefore, we speculated that the larger chirping rate on L2 than L1 may be due to the higher wave amplitude at the magnetic equator, which can be supported by the theoretical work by *Omura et al.* [2008].

Compared with previous 1-D PIC simulation results, our new simulation model exhibits several interesting properties of chorus waves in a 2-D frame. Due to the propagating effect, the wave normal angles of chorus waves are increasing during their propagation toward the higher-latitude regions along a enough curved field line as shown in Figures 9 and 10. This is qualitatively consistent with the results obtained from the ray tracing model [*Bortnik et al.*, 2011; *Breuillard et al.*, 2012; *Chen et al.*, 2012] and observation results [*Li et al.*, 2011b; *Agapitov et al.*, 2013]. In previous 1-D PIC simulation works, only the magnetic field line L2 is considered in their models [*Omura et al.*, 2008; *Hikishima and Omura*, 2012; *Katoh and Omura*, 2013; *Tao*, 2014]. However, along a curved magnetic field line (L1), the chirping rate of chorus waves is observed to be smaller than that along L2 (Figure 7) in our 2-D simulation model. Moreover, the threshold of electron temperature anisotropy to generate rising-tone chorus is significantly reduced after the assumptions of parallel propagation of chorus waves and parallel motion of electrons are released in a 2-D PIC simulation. With almost same plasma parameters, the electron temperature anisotropy  $T_{\perp\text{eq}}/T_{\parallel\text{eq}}$  to excite rising-tone chorus in a 1-D PIC simulation is required to be  $\sim 7$  [*Tao*, 2014], while that is reduced to  $\sim 3.8$  in our 2-D PIC simulation. This may suggest that the nonlinear interaction of chorus waves with hot electrons in the 2-D simulation is more efficient than that in the 1-D simulation. At this stage, our PIC code is only developed in a 2-D mirror field, which can be considered as an extension of previous simulation works. For the more practical purpose, we are trying to implement our PIC code in a 2-D or even 3-D dipole field.

#### Acknowledgments

The work at USTC was supported by the NSFC grants 41631071, 41331067, 41474125, 41604128, and 41421063, Key Research Program of Frontier Sciences CAS(QYZDJ-SSW-DQC010), and Youth Innovation Promotion Association of Chinese Academy of Sciences (2016395). The simulation data will be preserved on a long-term storage system and will be made available upon request to the corresponding authors.

#### References

- Agapitov, O., A. Artemyev, V. Krasnoselskikh, Y. V. Khotyaintsev, D. Mourenas, H. Breuillard, M. Balikhin, and G. Rolland (2013), Statistics of whistler-mode waves in the outer radiation belt: Cluster STAFF-SA measurements, *J. Geophys. Res. Space Physics*, *118*, 3407–3420, doi:10.1002/jgra.50312.
- Agapitov, O., A. Artemyev, D. Mourenas, V. Krasnoselskikh, J. Bonnell, O. Le Contel, C. M. Cully, and V. Angelopoulos (2014), The quasi-electrostatic mode of chorus waves and electron nonlinear acceleration, *J. Geophys. Res. Space Physics*, *119*, 1606–1626, doi:10.1002/2013JA019223.
- Artemyev, A. V., A. A. Vasiliev, D. Mourenas, O. V. Agapitov, V. Krasnoselskikh, D. Boscher, and G. Rolland (2014), Fast transport of resonant electrons in phase space due to nonlinear trapping by whistler waves, *Geophys. Res. Lett.*, *41*, 5727–5733, doi:10.1002/2014GL061380.
- Artemyev, A., O. Agapitov, D. Mourenas, V. Krasnoselskikh, V. Shastun, and F. Mozer (2016), Oblique whistler-mode waves in the Earth's inner magnetosphere: Energy distribution, origins, and role in radiation belt dynamics, *Space Sci. Rev.*, *200*, 261–355, doi:10.1007/s11214-016-0252-5.
- Bortnik, J., and R. M. Thorne (2007), The dual role of ELF/VLF chorus waves in the acceleration and precipitation of radiation belt electrons, *J. Atmos. Sol. Terr. Phys.*, *69*, 378–386, doi:10.1016/j.jastp.2006.05.030.
- Bortnik, J., L. Chen, W. Li, R. M. Thorne, N. P. Meredith, and R. B. Horne (2011), Modeling the wave power distribution and characteristics of plasmaspheric hiss, *J. Geophys. Res.*, *116*, A12209, doi:10.1029/2011JA016862.
- Breuillard, H., Y. Zaliznyak, V. Krasnoselskikh, O. Agapitov, A. Artemyev, and G. Rolland (2012), Chorus wave-normal statistics in the Earth's radiation belts from ray tracing technique, *Ann. Geophys.*, *30*, 1223–1233.
- Burtis, W. J., and R. A. Helliwell (1969), Banded chorus—A new type of VLF radiation observed in the magnetosphere by OGO 1 and OGO 3, *J. Geophys. Res.*, *74*, 3002–3010, doi:10.1029/JA074i011p03002.
- Cattell, C., et al. (2008), Discovery of very large amplitude whistler-mode waves in Earth's radiation belts, *Geophys. Res. Lett.*, *35*, L01105, doi:10.1029/2007GL032009.

- Chan, A. A., M. Xia, and L. Chen (1994), Anisotropic Alfvén-ballooning modes in Earth's magnetosphere, *J. Geophys. Res.*, *99*, 17,351–17,366, doi:10.1029/93JA03353.
- Chen, L., W. Li, J. Bortnik, and R. M. Thorne (2012), Amplification of whistler mode hiss inside the plasmasphere, *Geophys. Res. Lett.*, *39*, L08111, doi:10.1029/2012GL051488.
- Cornilleau-Wehrin, N., R. Gendrin, F. Lefeuvre, M. Parrot, R. Grard, D. Jones, A. Bahnsen, E. Ungstrup, and W. Gibbons (1978), VLF electromagnetic waves observed onboard GEOS-1, *Space Sci. Rev.*, *22*, 371–382, doi:10.1007/BF00210874.
- Cully, C. M., J. W. Bonnell, and R. E. Ergun (2008), THEMIS observations of long lived regions of large-amplitude whistler waves in the inner magnetosphere, *Geophys. Res. Lett.*, *35*, L17516, doi:10.1029/2008GL033643.
- Demekhov, A. G. (2011), Generation of VLF emissions with the increasing and decreasing frequency in the magnetospheric cyclotron maser in the backward wave oscillator regime, *Radiophys. Quantum Electron.*, *53*, 609–622, doi:10.1007/s11141-011-9256-x.
- Foster, J. C., P. J. Erickson, Y. Omura, D. N. Baker, C. A. Kletzing, and S. G. Claudepierre (2017), Van Allen Probes observations of prompt MeV radiation belt electron acceleration in nonlinear interactions with VLF chorus, *J. Geophys. Res. Space Physics*, *122*, 324–339, doi:10.1002/2016JA023429.
- Gao, X. L., W. Li, R. M. Thorne, J. Bortnik, V. Angelopoulos, Q. M. Lu, X. Tao, and S. Wang (2014a), New evidence for generation mechanisms of discrete and hiss-like whistler mode waves, *Geophys. Res. Lett.*, *41*, 4905–4811, doi:10.1002/2014GL060707.
- Gao, X. L., W. Li, R. M. Thorne, J. Bortnik, V. Angelopoulos, Q. M. Lu, X. Tao, and S. Wang (2014b), Statistical results describing the bandwidth and coherence coefficient of whistler mode waves using THEMIS waveform data, *J. Geophys. Res. Space Physics*, *119*, 8992–9003, doi:10.1002/2014JA020158.
- Gao, X. L., Q. M. Lu, J. Bortnik, W. Li, L. Chen, and S. Wang (2016a), Generation of multiband chorus by lower band cascade in the Earth's magnetosphere, *Geophys. Res. Lett.*, *43*, 2343–2350, doi:10.1002/2016GL068313.
- Gao, X. L., D. Mourenas, W. Li, A. V. Artemyev, Q. M. Lu, X. Tao, and S. Wang (2016b), Observational evidence of generation mechanisms for very oblique lower band chorus using THEMIS waveform data, *J. Geophys. Res. Space Physics*, *121*, 6732–6748, doi:10.1002/2016JA022915.
- Gao, X., Y. Ke, Q. Lu, L. Chen, and S. Wang (2017), Generation of multiband chorus in the Earth's magnetosphere: 1-D PIC simulation, *Geophys. Res. Lett.*, *44*, 618–624, doi:10.1002/2016GL072251.
- Gary, S. P., and H. Karimabadi (2006), Linear theory of electron temperature anisotropy instabilities: Whistler, mirror, and Weibel, *J. Geophys. Res.*, *111*, A11224, doi:10.1029/2006JA011764.
- Helliwell, R. A. (1967), A theory of discrete VLF emissions from the magnetosphere, *J. Geophys. Res.*, *72*, 4773–4790, doi:10.1029/JZ072i019p04773.
- Hikishima, M., and Y. Omura (2012), Particle simulations of whistler-mode rising-tone emissions triggered by waves with different amplitudes, *J. Geophys. Res.*, *117*, A04226, doi:10.1029/2011JA017428.
- Horne, R. B., S. A. Glauert, and R. M. Thorne (2003), Resonant diffusion of radiation belt electrons by whistler mode chorus, *Geophys. Res. Lett.*, *30*(9), 1493, doi:10.1029/2003GL016963.
- Horne, R. B., R. M. Thorne, S. A. Glauert, J. M. Albert, N. P. Meredith, and R. R. Anderson (2005), Timescale for radiation belt electron acceleration by whistler mode chorus waves, *J. Geophys. Res.*, *110*, A03225, doi:10.1029/2004JA010811.
- Karpman, V. I., J. N. Istomin, and D. R. Shklyar (1974), Nonlinear frequency shift and self-modulation of the quasi-monochromatic whistlers in the inhomogeneous plasma (magnetosphere), *Planet. Space Sci.*, *22*, 859–871, doi:10.1016/0032-0633(74)90155-X.
- Katoh, Y., and Y. Omura (2006), A study of generation mechanism of VLF triggered emission by self-consistent particle code, *J. Geophys. Res.*, *111*, A12207, doi:10.1029/2006JA011704.
- Katoh, Y., and Y. Omura (2007), Computer simulation of chorus wave generation in the Earth's inner magnetosphere, *Geophys. Res. Lett.*, *34*, L03102, doi:10.1029/2006GL028594.
- Katoh, Y., and Y. Omura (2013), Effect of the background magnetic field inhomogeneity on generation processes of whistler-mode chorus and broadband hiss-like emissions, *J. Geophys. Res. Space Physics*, *118*, 4189–4198, doi:10.1002/jgra.50395.
- Kellogg, P. J., C. A. Cattell, K. Goetz, S. J. Monson, and L. B. Wilson III (2011), Large amplitude whistlers in the magnetosphere observed with Wind-Waves, *J. Geophys. Res.*, *116*, A09224, doi:10.1029/2010JA015919.
- Koons, H. C. (1981), The role of hiss in magnetospheric chorus emissions, *J. Geophys. Res.*, *86*, 6745–6754, doi:10.1029/JA086iA08p06745.
- Koons, H. C., and J. L. Roeder (1990), A survey of equatorial magnetospheric wave activity between 5 and 8  $R_E$ , *Planet. Space Sci.*, *38*(10), 1335–1341, doi:10.1016/0032-0633(90)90136-E.
- Lam, M. M., R. B. Horne, N. P. Meredith, S. A. Glauert, T. Moffat-Griffin, and J. C. Green (2010), Origin of energetic electron precipitation >30 keV into the atmosphere, *J. Geophys. Res.*, *115*, A00F08, doi:10.1029/2009JA014619.
- Lauben, D. S., U. S. Inan, T. F. Bell, and D. A. Gurnett (2002), Source characteristics of ELF/VLF chorus, *J. Geophys. Res.*, *107*(A12), 1429, doi:10.1029/2000JA003019.
- LeDocq, M. J., D. A. Gurnett, and G. B. Hospodarsky (1998), Chorus source locations from VLF Poynting flux measurements with the Polar spacecraft, *Geophys. Res. Lett.*, *25*, 4063–4066, doi:10.1029/1998GL900071.
- Li, W., R. M. Thorne, V. Angelopoulos, J. W. Bonnell, J. P. McFadden, C. W. Carlson, O. LeContel, A. Roux, K. H. Glassmeier, and H. U. Auster (2009), Evaluation of whistler-mode chorus intensification on the nightside during an injection event observed on the THEMIS spacecraft, *J. Geophys. Res.*, *114*, A00C14, doi:10.1029/2008JA013554.
- Li, W., et al. (2010), THEMIS analysis of observed equatorial electron distributions responsible for the chorus excitation, *J. Geophys. Res.*, *115*, A00F11, doi:10.1029/2009JA014845.
- Li, W., R. M. Thorne, J. Bortnik, Y. Y. Shprits, Y. Nishimura, V. Angelopoulos, C. Chaston, O. LeContel, and J. W. Bonnell (2011b), Typical properties of rising and falling tone chorus waves, *Geophys. Res. Lett.*, *38*, L14103, doi:10.1029/2011GL047925.
- Li, W., J. Bortnik, R. M. Thorne, and V. Angelopoulos (2011a), Global distribution of wave amplitudes and wave normal angles of chorus waves using THEMIS wave observations, *J. Geophys. Res.*, *116*, A12205, doi:10.1029/2011JA017035.
- Li, W., R. M. Thorne, J. Bortnik, X. Tao, and V. Angelopoulos (2012), Characteristics of hiss-like and discrete whistler mode emissions, *Geophys. Res. Lett.*, *39*, L18106, doi:10.1029/2012GL053206.
- Li, W., et al. (2014), Radiation belt electron acceleration by chorus waves during the 17 March 2013 storm, *J. Geophys. Res. Space Physics*, *119*, 4681–4693, doi:10.1002/2014JA019945.
- Lorentzen, K. R., J. B. Blake, U. S. Inan, and J. Bortnik (2001), Observations of relativistic electron microbursts in association with VLF chorus, *J. Geophys. Res.*, *106*, 6017–6027, doi:10.1029/2000JA003018.
- Meredith, N. P., R. B. Horne, and R. R. Anderson (2001), Substorm dependence of chorus amplitudes: Implications for the acceleration of electrons to relativistic energies, *J. Geophys. Res.*, *106*, 13,165–13,178, doi:10.1029/2000JA900156.
- Ni, B., R. M. Thorne, N. P. Meredith, R. B. Horne, and Y. Y. Shprits (2011a), Resonant scattering of plasma sheet electrons leading to diffuse auroral precipitation: 2. Evaluation for whistler mode chorus waves, *J. Geophys. Res.*, *116*, A04219, doi:10.1029/2010JA016233.

- Ni, B., R. M. Thorne, N. P. Meredith, Y. Y. Shprits, and R. B. Horne (2011b), Diffuse auroral scattering by whistler mode chorus waves: Dependence on wave normal angle distribution, *J. Geophys. Res.*, *116*, A10207, doi:10.1029/2011JA016517.
- Nunn, D. (1971), A theory of VLF emissions, *Planet. Space Sci.*, *19*, 1141–1167, doi:10.1016/0032-0633(71)90110-3.
- Nunn, D. (1974), A self-consistent theory of triggered VLF emissions, *Planet. Space Sci.*, *22*, 349–378, doi:10.1016/0032-0633(74)90070-1.
- Nunn, D., and Y. Omura (2012), A computational and theoretical analysis of falling frequency VLF emissions, *J. Geophys. Res.*, *117*, A08228, doi:10.1029/2012JA017557.
- Nunn, D., and Y. Omura (2015), A computational and theoretical investigation of nonlinear wave-particle interactions in oblique whistlers, *J. Geophys. Res. Space Physics*, *120*, 2890–2911, doi:10.1002/2014JA020898.
- Nunn, D., Y. Omura, H. Matsumoto, I. Nagano, and S. Yagitani (1997), The numerical simulation of VLF chorus and discrete emissions observed on the Geotail satellite using a Vlasov code, *J. Geophys. Res.*, *102*, 27,083–27,097, doi:10.1029/97JA02518.
- Omura, Y., and D. Nunn (2011), Triggering progress of whistler mode chorus emissions in the magnetosphere, *J. Geophys. Res.*, *116*, A05205, doi:10.1029/2010JA016280.
- Omura, Y., and H. Matsumoto (1982), Computer simulations of basic processes of coherent whistler wave-particle interactions in the magnetosphere, *J. Geophys. Res.*, *87*, 4435–4444, doi:10.1029/JA087iA06p04435.
- Omura, Y., and D. Summers (2006), Dynamics of high-energy electrons interacting with whistler mode chorus emissions in the magnetosphere, *J. Geophys. Res.*, *111*, A09222, doi:10.1029/2006JA011600.
- Omura, Y., N. Furuya, and D. Summers (2007), Relativistic turning acceleration of resonant electrons by coherent whistler mode waves in a dipole magnetic field, *J. Geophys. Res.*, *112*, A06236, doi:10.1029/2006JA012243.
- Omura, Y., Y. Katoh, and D. Summers (2008), Theory and simulation of the generation of whistler-mode chorus, *J. Geophys. Res.*, *113*, A04223, doi:10.1029/2007JA012622.
- Omura, Y., D. Nunn, and D. Summers (2012), Generation processes of whistler mode chorus emissions: Current status of nonlinear wave growth theory, in *Dynamics of the Earth's Radiation Belts and Inner Magnetosphere*, *Geophys. Monogr. Ser.*, vol. 199, edited by D. Summers, et al., pp. 243–254, AGU, Washington, D. C., doi:10.1029/2012GM001347.
- Pope, J. H. (1963), A high-latitude investigation of the natural very-low-frequency electromagnetic radiation known as chorus, *J. Geophys. Res.*, *68*, 83–99, doi:10.1029/JZ068i001p00083.
- Santolik, O., D. A. Gurnett, J. S. Pickett, M. Parrot, and N. Cornilleau-Wehrin (2003), Spatio-temporal structure of storm-time chorus, *J. Geophys. Res.*, *108*(A7), 1278, doi:10.1029/2002JA009791.
- Santolik, O., D. A. Gurnett, J. S. Pickett, M. Parrot, and N. Cornilleau-Wehrin (2005), Central position of the source region of storm-time chorus, *Planet. Space Sci.*, *53*, 299–305, doi:10.1016/j.pss.2004.09.056.
- Santolik, O., D. A. Gurnett, J. S. Pickett, J. Chum, and N. Cornilleau-Wehrin (2009), Oblique propagation of whistler mode waves in the chorus source region, *J. Geophys. Res.*, *114*, A00F03, doi:10.1029/2009JA014586.
- Shklyar, D., and H. Matsumoto (2009), Oblique whistler-mode waves in the inhomogeneous magnetospheric plasma: Resonant interactions with energetic charged particles, *Surv. Geophys.*, *30*, 55–104, doi:10.1007/s10712-009-9061-7.
- Summers, D., R. M. Thorne, and F. L. Xiao (1998), Relativistic theory of wave-particle resonant diffusion with application to electron acceleration in the magnetosphere, *J. Geophys. Res.*, *103*, 20,487–20,500, doi:10.1029/98JA01740.
- Summers, D., B. Ni, and N. P. Meredith (2007), Timescales for radiation belt electron acceleration and loss due to resonant wave-particle interactions: 2. Evaluation for VLF chorus, ELF hiss, and electromagnetic ion cyclotron waves, *J. Geophys. Res.*, *112*, A04207, doi:10.1029/2006JA011993.
- Tao, X. (2014), A numerical study of chorus generation and the related variation of wave intensity using the DAWN code, *J. Geophys. Res. Space Physics*, *119*, 3362–3372, doi:10.1002/2014JA019820.
- Thorne, R. M. (2010), Radiation belt dynamics: The importance of wave-particle interactions, *Geophys. Res. Lett.*, *37*, L22107, doi:10.1029/2010GL044990.
- Thorne, R. M., T. P. O'Brien, Y. Y. Shprits, D. Summers, and R. B. Horne (2005), Timescale for MeV electron microburst loss during geomagnetic storms, *J. Geophys. Res.*, *110*, A09202, doi:10.1029/2004JA010882.
- Thorne, R. M., B. Ni, X. Tao, R. B. Horne, and N. P. Meredith (2010), Scattering by chorus waves as the dominant cause of diffuse auroral precipitation, *Nature*, *467*, 943–946, doi:10.1038/nature09467.
- Thorne, R. M., et al. (2013), Rapid local acceleration of relativistic radiation-belt electrons by magnetospheric chorus, *Nature*, *504*(7480), 411, doi:10.1038/Nature12889.
- Tsurutani, B. T., and E. J. Smith (1974), Postmidnight chorus: A substorm phenomenon, *J. Geophys. Res.*, *79*, 118–127, doi:10.1029/JA079i001p00118.
- Tsurutani, B. T., and E. J. Smith (1977), Two types of magnetospheric ELF chorus and their substorm dependences, *J. Geophys. Res.*, *82*, 5112–5128, doi:10.1029/JA082i032p05112.
- Wilson, L. B., III, C. A. Cattell, P. J. Kellogg, J. R. Wygant, K. Goetz, A. Breneman, and K. Kersten (2011), The properties of large amplitude whistler mode waves in the magnetosphere: Propagation and relationship with geomagnetic activity, *Geophys. Res. Lett.*, *38*, L17107, doi:10.1029/2011GL048671.